



Detoxification and selective separation of Cr(VI) and As(III) in wastewater based on interfacial coupling in BiOBr with {110} facet under visible-light irradiation

Tong Li^{a,b}, Lili Zhang^c, Yaowen Gao^b, Xueci Xing^b, Xiaohan Zhang^b, Fan Li^{b,*}, Chun Hu^b

^a School of Energy and Environmental Engineering, University of Science and Technology Beijing, Beijing 100083, China

^b Key Laboratory for Water Quality and Conservation of the Pearl River Delta, Ministry of Education, Institute of Environmental Research at Greater Bay, Guangzhou University, Guangzhou 510006, China

^c Key Laboratory of Drinking Water Science and Technology, Research Center for Eco-Environmental Sciences, Chinese Academy of Sciences, Beijing 100085, China

ARTICLE INFO

Keywords:

Layered structural BiOBr
Interlayer ion exchange
Interfacial coupling
Synergic removal
Selective separation of chromium and arsenic

ABSTRACT

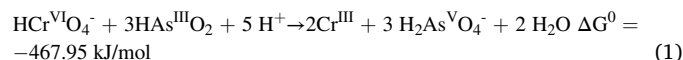
Layered structural BiOBr with {110} facet exposure is a promising functional material for highly selective adsorption and separation of heavy metal ions in water purification. In this study, the distinct adsorption behaviors of As(III), As(V), and Cr(VI) on {110} facet were theoretically and experimentally investigated. The results suggested that uncharged As(III) was dominantly adsorbed on the $[\text{Bi}_2\text{O}_2]^{2+}$ surface replacing the hydroxyl group, whereas Cr(VI) and As(V) oxyanions preferentially intercalated on {110} facet by exchange with Br^- ions between the layers. Moreover, due to interfacial coupling configuration ($[\text{BiO-CrO}_4\text{-O}]\text{-O-As(OH)}_2$) between the surface and interlayer on {110} facet, the synergic removal of Cr(VI) and As(III) could be accelerated under photoexcitation to induce a direct electron transfer from surface As^{III} to interlayer Cr^{VI} , forming As^{V} and Cr^{III} . Subsequently, approximately 69.3% of Cr(III) and 98.6% of As(V) were readily desorbed in acidic conditions and a high concentration of Br^- solution, respectively, to achieve simultaneous detoxification and selective separation.

1. Introduction

Arsenic (As) and chromium (Cr), the major carcinogenic contaminants in industrial wastewater, pose significant threats to underground water resources and human living [1]. The combined pollution caused by As and Cr in the form of oxyanion species (CrO_4^{2-} [Cr(VI)], AsO_3^{3-} [As(III)], and AsO_4^{3-} [As(V)]) commonly coexist in acid mine drainage (AMD) and wood preservative wastewater [2]. The high mobility and solubility characteristics are becoming increasingly critical environmental concerns [3]. As(V) is considered much less toxic and more accessible to be removed by various adsorbents than As(III) [4–6]. Comparatively, highly poisonous Cr(VI) can effectively transform into a non-toxic and insoluble Cr(OH)_3 precipitate over a wide pH range. Therefore, the reduction of Cr(VI) to Cr(III) and oxidation of As(III) to As(V) in synchronism, followed by the adsorption or coagulation treatments, is conducive to immobilizing As and Cr with much lower toxicity.

The direct simultaneous redox reaction is negligibly slow under neutral conditions, as shown in Eq. (1), owing to the involvement of H^+

in the reaction [7]. Likewise, H_2O_2 can be utilized as an intermediate redox-active substance to achieve the synchronized conversion of Cr(VI) and As(III) under acidic conditions ($\text{pH} = 3$). Because of the intermediate $\text{Cr(V)}/\text{H}_2\text{O}_2$ Haber-Weiss-type reactions, the formation of $\bullet\text{OH}$ radicals was primarily responsible for oxidizing As(III) [8]. However, it was still severely limited by the pH value of the solution owing to the low redox potential of $\text{E}^0(\text{HCr}^{\text{VI}}\text{O}_4^-/\text{Cr}^{3+})$ in Eq. (2) [9]. Other methods, including mackinawite (FeS) [10], ferrihydrite [11], and non-thermal discharge plasma [12], have been proposed to transform Cr(VI) and As(III), but treatment efficiency is also restrained by specific reaction conditions and massive energy consumption. Hence, developing highly efficient technologies for simultaneous conversion of As(III) and Cr(VI) over a wide pH range remains a great challenge.



* Corresponding author.

E-mail address: lifan@gzhu.edu.cn (F. Li).

<https://doi.org/10.1016/j.apcatb.2022.121192>

Received 26 November 2021; Received in revised form 28 January 2022; Accepted 4 February 2022

Available online 8 February 2022

0926-3373/© 2022 Elsevier B.V. All rights reserved.

Photocatalysts, such as TiO_2 [13–16], C_3N_4 [17–19], and Fe-based photocatalysts [20], have been widely applied for Cr(VI) reduction and As(III) oxidation, depending on the photogenerated electron (e^-) and hole (h^+) pairs, respectively. Nevertheless, the interfacial charge transfer and optoelectronic properties restrict the cooperative conversion efficiency under neutral conditions. Furthermore, additional adsorbents are indispensable for the removal of the later formed As(V) products [21,22]. Recently, researchers have found that BiOBr consisting of $[\text{Bi}_2\text{O}_2]^{2+}$ and double $[\text{Br}_2]^{2-}$ slabs exhibits excellent performance for oxyanion adsorption because of the interlayer anion exchange [23]. Owing to the weak nonbonding (van der Waals) interaction of the $[\text{Br}_2]^{2-}$ layer, oxyanions can be easily exchanged with Br^- between layers [24]. BiOBr with $\{110\}$ facet has been identified as an anion-exchange channel for oxyanion (CrO_4^{2-}) intercalation between layers, in contrast to the $\{001\}$ facet, which has a higher surface charge separation efficiency [25,26]. Furthermore, the intercalated CrO_4^{2-} doping provided Cr 3d states as acceptor levels to change the energy band structure of BiOBr, which made electrons directly transferred into the Cr 3d states for Cr(VI) reduction without H^+ involvement [26]. Based on the unique interfacial properties of the $\{110\}$ facet (interlayer and surface) [27], BiOBr photocatalysts are perceived as promising candidates for simultaneous redox conversion of Cr(VI) and As(III), as well as the removal of later formed As(V).

Considering the species distribution as a function of pH, the adsorption behaviors of Cr(VI), As(III), and As(V) have been investigated on the $\{110\}$ -facet dominant BiOBr to determine the facet-dependent redox-active sites. Moreover, simultaneous Cr(VI) reduction and As(III) oxidation, along with the removal of in situ formed As(V) are carried out in the $\{110\}$ -facet dominant BiOBr photocatalytic system, and the mechanism involved in interfacial coupling between the surface and interlayer is proposed accordingly. Our research provides new insight into the role of the $\{110\}$ facet in the synergic removal and selective separation of chromium and arsenic heavy metals by BiOBr in a facile and efficient approach.

2. Materials and methods

2.1. Preparation of BiOBr exposed with $\{110\}$ facets

BiOBr was synthesized following the modified method proposed by Li et al. [26,28]. The facet-controllable synthesis of BiOBr nanosheets with high $\{110\}$ facet exposure percentages could be achieved by adjusting the pH of the precursor solution, defined as 110-BiOBr. Briefly, 0.485 g of $\text{Bi}(\text{NO}_3)_3 \cdot 5\text{H}_2\text{O}$ and 30 mmol of NaBr were added to 40 mL of mannitol solution (0.1 M) with continuous stirring. Subsequently, 1 M NaOH solution was carefully dropped into the aforementioned solution until the pH value reached 6.0, forming homogeneous white suspensions. After heating at 160 °C for 3 h, the white powder products of 110-BiOBr were washed with deionized water and methanol and dried at 60 °C in an oven.

2.2. Characterization

Powder X-ray diffraction (XRD) measurements were carried out with Cu K α radiation ($\lambda = 1.540598 \text{ \AA}$) operated at 40 kV and 40 mA (PANalytical X'Pert Pro). The morphology of the samples was observed by high-resolution transmission electron microscopy (HRTEM) with an accelerating voltage of 200 kV (JEOL JEM-2010). X-ray photoelectron spectroscopy (XPS) was used to analyze the chemical composition of the samples (Thermo ESCALAB 250Xi) with monochromatic Al K α radiation (225 W, 15 mA, 15 kV), and the binding energy (BE) was calibrated with the C 1 s peak at 284.6 eV. Raman spectroscopic measurements were conducted using a confocal laser micro-Raman spectrometer with a 633 nm laser light (Thermo DXR).

2.3. Adsorption isotherms

The adsorption isotherms of As(III), As(V), and Cr(VI) at different pH of 5.0, 7.0, and 9.0 were conducted by 25.0 mg of 110-BiOBr samples in 50 mL with different initial concentrations, i.e., 5, 15, 30, 45, 60, 75 and 90 mg/L. All suspensions were sealed and stirred in a constant temperature shaker ($25 \pm 1 \text{ }^\circ\text{C}$) for 24 h. Subsequently, the samples were filtered through a 0.45- μm membrane to measure the residual concentrations of Cr(VI), As(III), and As(V) in solution. The adsorption capacities (Q_e) for As(III), As(V), and Cr(VI) were calculated on the basis of Eq. (3).

$$Q_e = \frac{V(C_0 - C_e)}{m} \quad (3)$$

where Q_e (mg/g) is the equilibrium adsorption capacity; C_0 and C_e (mg/L) represent the initial and equilibrium concentrations of adsorbates in the solution, respectively; V (mL) is the volume of the aqueous solution; and m (mg) denotes the mass of the adsorbent used in the experiment. The concentrations of As(III), As(V), and Cr(VI) were analyzed using inductively coupled plasma-optical emission spectrometry (ICP-OES) (Agilent 5100). Additionally, the adsorbents were separated by centrifugation to further characterize the surface adsorption properties of 110-BiOBr with Cr(VI), As(III), and As(V).

2.4. Photocatalytic simultaneous Cr(VI) reduction and As(III) oxidation test

The photocatalytic activity experiments of Cr(VI) reduction and As(III) oxidation were performed at ambient temperature using a 500 W Xe arc lamp with a 420 nm cut-off filter as the light source. Typically, 25.0 mg quantity of BiOBr was added to 50 mL of 10 mg/L Cr(VI), 10 mg/L As(III), and a mixed aqueous solution containing 10 mg/L Cr(VI) and 10 mg/L As(III), respectively. Before irradiation, the suspensions were stirred in the dark for 0.5 h to ensure adsorption/desorption equilibrium. The Cr(VI) concentration in the solution was measured using the 1,5-diphenylcarbazid analytical method at 540 nm using a UV-Vis spectrophotometer (Hitachi U-4100). The concentrations of As(III) and As(V) were determined by inductively coupled plasma mass spectrometry (PerkinElmer Optima 2000).

3. Results and discussion

3.1. Characterization of the as-prepared 110-BiOBr

Based on the reported method, BiOBr nanosheets exposed with $\{110\}$ facet were synthesized as 110-BiOBr [25]. The XRD patterns of 110-BiOBr showed distinctly high $\{110\}$ peaks relative to that of $\{001\}$ [26], indicating 110-BiOBr with high $\{110\}$ facet exposure percentages (Fig. S1). The high-resolution transmission electron microscopy (HRTEM) displayed the sheet-shaped morphology of 110-BiOBr with a size of about 100 nm (Fig. S2a). The continuous lattice fringes were measured as 0.27, 0.26, and 0.23 nm, indexed to (111), (003), and (112) atomic planes, respectively (Fig. S2b). The corresponding SAED pattern indicated angles of adjacent spots at 71° and 55° (Fig. S2c), identified as the theoretical values associated with (003) planes between two other planes ((111) and (112)). These results revealed that the $\{110\}$ facet was dominantly exposed on the surface of BiOBr nanosheets. As shown in the geometric structure of 110-BiOBr (Fig. S3), the $\{110\}$ facet of BiOBr provided abundant anion exchange channels between layers, whereas the (001) facet displayed the covalent bonding of $[\text{Bi}_2\text{O}_2]^{2+}$ layers with a strong internal electric field (IEF) [29,30].

3.2. Adsorption behaviors of Cr(VI), As(III), and As(V) on 110-BiOBr samples

According to the distinctive interface properties of the {110} facet, adsorption experiments of As(III), As(V), and Cr(VI) were carried out on 110-BiOBr to explore the facet-dependent adsorption sites. Based on the arsenic species distribution as a function of pH [22,31], As(III) mainly exists as uncharged species (H_3AsO_3) in a wide pH range from 5 to 9 (Fig. 1a), whereas As(V) presents as the oxyanions of H_2AsO_4^- at pH 2.0–6.8 and HAsO_4^{2-} at pH 6.8–11.0 (Fig. 1b). Similarly, Cr(VI) is

pH-dependent and exists in the form of dichromate ($\text{Cr}_2\text{O}_7^{2-}$) at pH < 2, hydrogen chromate (HCrO_4^-) at pH 4–6, and chromate (CrO_4^{2-}) at 6–12, respectively (Fig. 1c) [32]. Thus, the dominant Cr(VI) and As(V) species are negatively charged ions at pH 5–9, which is different from electrically neutral As(III).

Fig. 2 shows the adsorption isotherms of As(III), As(V), and Cr(VI) on 110-BiOBr at different pH values (5.0, 7.0, and 9.0) at 25 °C. The adsorption amounts of As(III) gradually enhanced with increasing initial concentrations in the solution. The optimum pH for As(III) adsorption was observed at pH 7.0, ascribed to the substitution of hydroxyl groups ($\equiv\text{OH}$) on the 110-BiOBr surface with uncharged H_3AsO_3 . Moreover, the protonation of $\equiv\text{OH}$ ($\equiv\text{OH}_2^+$) tended to decrease the As(III) adsorption at pH 5.0 [33]. At a high pH of 9.0, the charge repulsion between the surface $\equiv\text{O}^-$ groups and negatively charged H_2AsO_3^- significantly inhibited As(III) adsorption on 110-BiOBr. Therefore, we inferred that As(III) was preferentially adsorbed on the 110-BiOBr surface, depending on the surface $\equiv\text{OH}$ groups of $[\text{Bi}_2\text{O}_2]^{2+}$ layer.

The equilibrium adsorption isotherm data were fitted by the Langmuir (Eq. (4)) and Freundlich isotherm models (Eq. (5)), respectively.

$$Q_e = \frac{q_m k_L C_e}{1 + k_L C_e} \quad (4)$$

$$Q_e = k_F (C_e)^{\frac{1}{n}} \quad (5)$$

where Q_e (mg/g) is the adsorption capacity of metal ions at equilibrium, and C_e (mg/L) denotes the equilibrium concentration of metal ions in solution.

In the Langmuir isotherm, k_L (L/mg) represents the free energy of sorption, and q_m (mg/g) is the maximum adsorption capacity. The k_F (mg/g) and n in the Freundlich isotherm are quantitatively indicative of the adsorption capability of the adsorbents. According to the correlation coefficients (R^2), the Langmuir model was more appropriate than the Freundlich model for describing As(III) adsorption on 110-BiOBr samples (Table 1), indicating that the adsorption process of As(III) was likely as a monolayer on the surface.

On the contrary, the adsorption amount of As(V) on 110-BiOBr almost kept a constant value near 20.1 mg/g at pH 5.0, which was uncorrelated with the initial As(V) concentration ($[\text{As(V)}]_0$) in the solution. Notably, 5.0 mg/L of $[\text{As(V)}]_0$ was a particular case, in which the As(V) adsorption capacity was as low as 10.0 mg/g because all As(V) in the solution was entirely adsorbed on 110-BiOBr. These results illustrated that the {110} facet of 110-BiOBr possessed a certain number of adsorption sites for As(V) species (H_2AsO_4^- and HAsO_4^{2-}) derived from interlayer anionic zones. Moreover, the adsorption amount of As(V) at pH 7.0 declined markedly, which might be attributed to HAsO_4^{2-} with more negative charges taking up more sites. Additionally, As(V) adsorption gradually increased from 8.0 to 23.0 mg/g with increasing $[\text{As(V)}]_0$ at pH 9.0. To the best of our knowledge, halogen atoms could be gradually exchanged and occupied by OH^- to form non-stoichiometric oxides such as $[\text{Bi}_7\text{O}_9]^{3+}$, $[\text{Bi}_{12}\text{O}_{15}]^{6+}$, and $[\text{Bi}_{24}\text{O}_{31}]^{10+}$ under alkaline pH conditions [34]. Owing to the variable crystal configurations and charges in the $[\text{BiO}]^{n+}$ layer, the interlayer anionic zones also underwent a corresponding transformation, leading to the increased As(V) adsorption at pH 9.0.

Interestingly, Cr(VI) adsorption on 110-BiOBr exhibited a trend similar to that of As(V), and the adsorption amount of Cr(VI) was maintained at 10.8 mg/g at pH 7.0, irrespective of the initial Cr(VI) concentration (Fig. S4). Cr(VI) was mainly intercalated into interlayers by anion exchange with $[\text{Br}_2]^{2-}$ (Fig. S5), relying heavily on {110} facet exposure [24,26]. The same phenomenon was observed for As(V) and Cr(VI), demonstrating that the adsorption behavior of As(V) oxyanion species was utterly consistent with Cr(VI) that intercalated in the interlayer anionic area. Furthermore, the introduction of Cr(VI) negatively affected As(V) adsorption, but had a negligible effect on As(III) because of competitive adsorption between As(V) and Cr(VI) anion

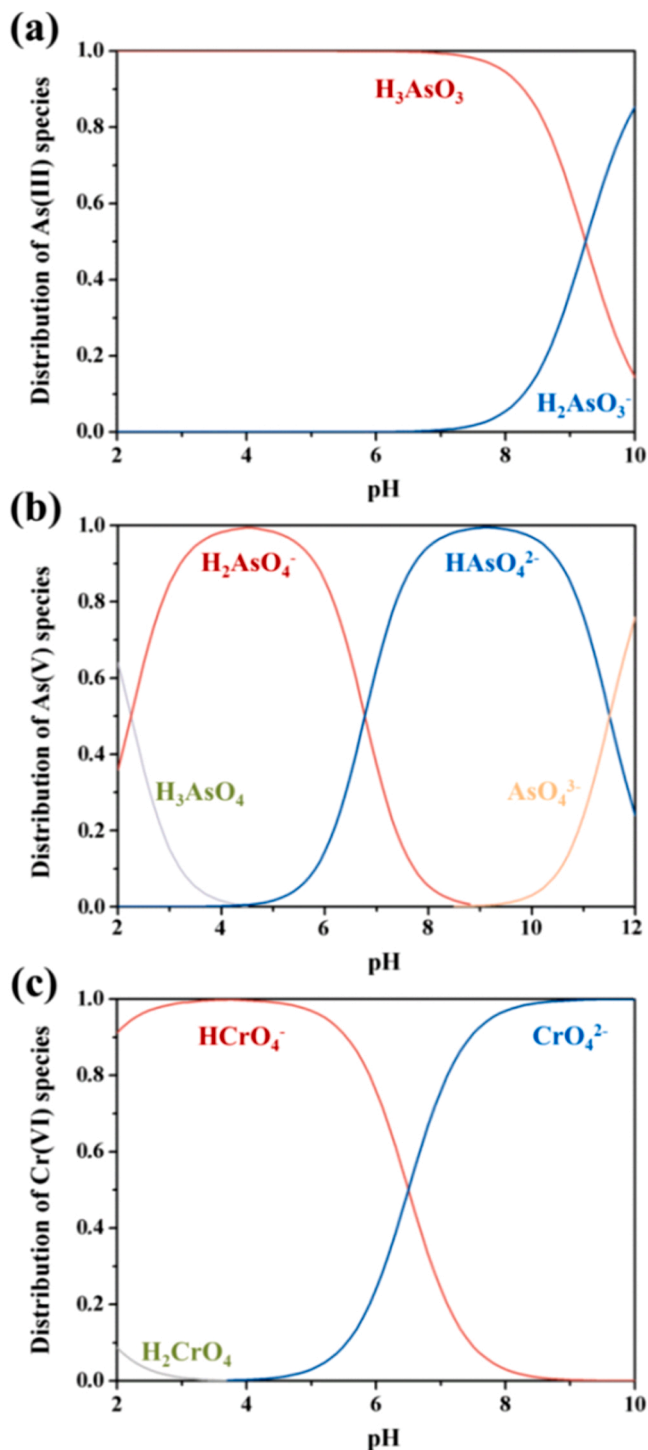


Fig. 1. The speciation distribution of As(III) (a), As(V) (b) and Cr(VI) (c) as a function of pH.

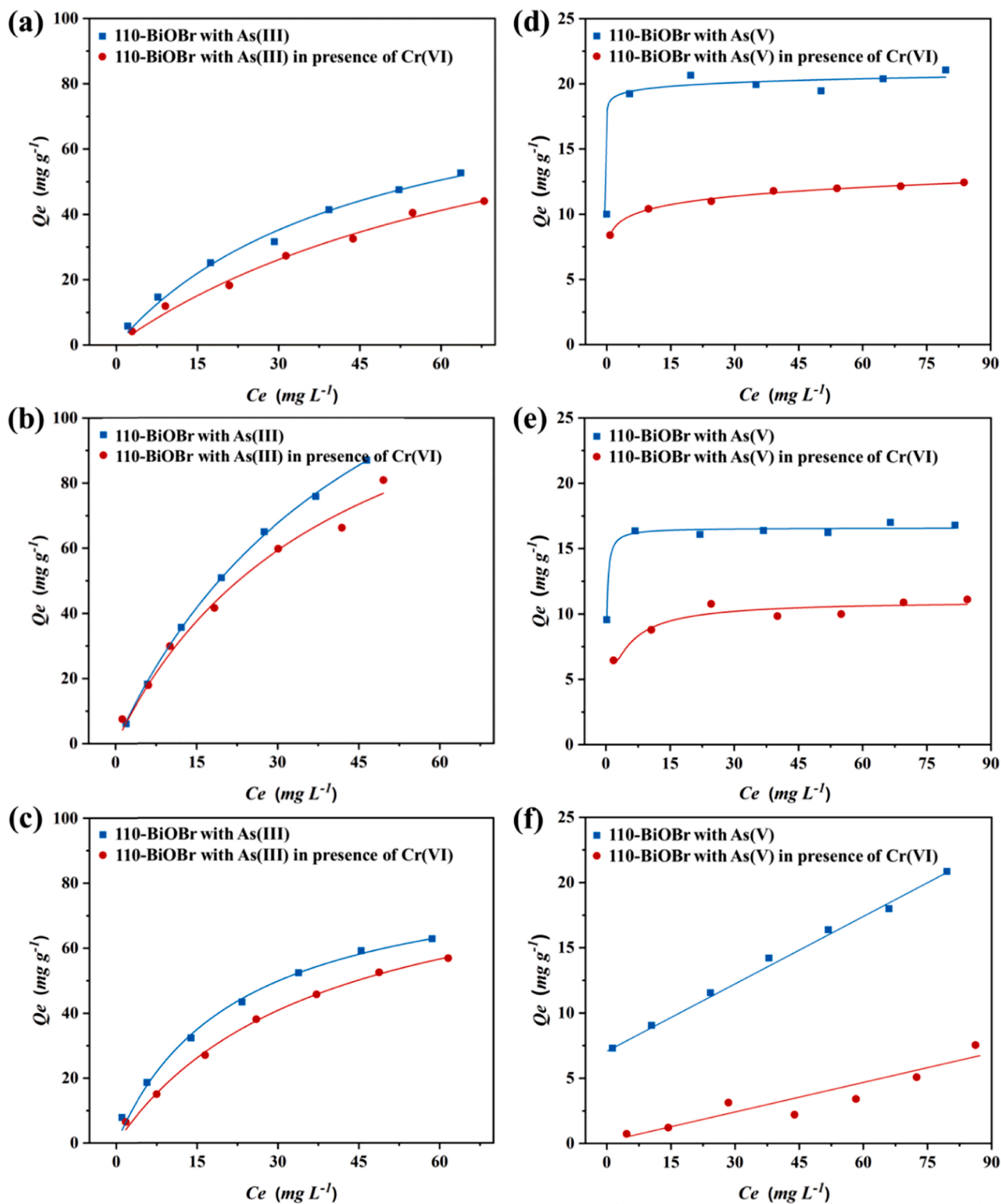


Fig. 2. Adsorption isotherm in different pH conditions (5, 7, 9) of As(III) (a-c), As(V) (d-f) on 110-BiOBr samples with and without Cr(VI). Initial As(III) and As(V) concentration was 10–90 mg/L; the adsorbent dose was 0.4 g/L; the solution volume was 50 mL.

species. Accordingly, a remarkable decrease of Cr(VI) adsorption on 110-BiOBr was also observed in the presence of As(V) rather than As(III) (Fig. S6).

3.3. Intrinsic adsorption mechanism

The FTIR spectra of 110-BiOBr samples before and after As(III) and As(V) adsorption are shown in Fig. 3a. The peak at 528 cm^{-1} was assigned to the $\sigma(\text{Bi-O})$ stretching mode of 110-BiOBr [35]. Obviously, As(III) adsorption on 110-BiOBr mainly caused a significant redshift of

Table 1

Comparison of the fitted data involved in the adsorption of As(III) on 110-BiOBr.

As (III) Adsorption		Langmuir model			Freundlich model		
		q_m (mg/g)	k_L (L/mg)	R^2	k_F	n	R^2
pH 5	110-BiOBr	81.85	0.024	0.986	4.43	1.69	0.98
	110-BiOBr-Cr	66.54	0.015	0.977	1.94	1.54	0.977
	110-BiOBr	159.59	0.020	0.999	6.02	1.42	0.993
pH 7	110-BiOBr	132.78	0.014	0.994	3.21	1.37	0.983
	110-BiOBr	101.5	0.006	0.981	0.85	1.18	0.973
pH 9	110-BiOBr	86.65	0.045	0.994	8.77	2.02	0.993
	110-BiOBr-Cr						

the $\sigma(\text{Bi-O})$ peak from 528 to 516 cm^{-1} , indicating that the non-ionic As(III) molecules adsorbed on the surface of $[\text{Bi}_2\text{O}_2]^{2+}$ layer induced the vibration of the Bi-O bond. Comparatively, it showed little variation upon 110-BiOBr with adsorbed As(V), yet a newly emerged peak at 769 cm^{-1} belonging to As-O vibration was obtained [35]. The variation of As-O vibration was associated with the intercalated As(V) in the {110} facet. The Raman spectra exhibited four distinctive peaks at 52, 90, 113, and 162 cm^{-1} , which were indexed to A_{1g} external Bi-Br stretching, E_g external Bi-Br stretching, A_{1g} internal Bi-Br stretching, and E_g internal Bi-Br stretching, respectively [36,37]. Moreover, two additional weak peaks at 846 and 938 cm^{-1} , corresponding to the symmetric and asymmetric stretching vibrations of As-O (Fig. 3b), were observed for 110-BiOBr with the adsorbed As(V) rather than As(III). These results suggested that the vibration of the As-O peaks might be derived from the adsorbed As(V) between the layers.

The XPS results provided further information on the interfacial interactions between As(III)/As(V)/Cr(VI) and 110-BiOBr. The appearance of As 3d peak was identified in Fig. 4a, confirming the adsorption of As(III) and As(V) on 110-BiOBr samples. The distinct peaks of As(III) and As(V) binding energies were appeared at 44.4 and 44.8 eV, respectively. The corresponding ratios of adsorbed oxygen (O-adsorbed at 531.1 eV) and lattice oxygen (O-lattice at 529.9 eV), that is, O-adsorbed/O-lattice, remarkably increased from 18.7% to 42.5% after As(III) adsorption (Fig. 4b). The strengthened intensity of O-adsorbed peak was mostly ascribed to As(III) replaced with surface $\equiv\text{OH}$ on the $[\text{Bi}_2\text{O}_2]^{2+}$ layer, forming a Bi-O-As(OH)₂ structure. Regarding the As(V) adsorption, the

O-lattice peak at 529.9 shifted to 530.1 eV, whereas the O-adsorbed/O-lattice ratio has only a slight increase accordingly. These results suggested that the intercalated As(V) between layers via a facile exchange with $[\text{Br}_2]^{2-}$ layers is highly likely to form a $\text{Bi}_2\text{O}_2\text{-HAsO}_4$ structure ($[\text{BiO-HAsO}_4\text{-O}]\text{Bi}$), which caused the $[\text{Bi}_2\text{O}_2]^{2+}$ layer conversion, leading to the movement of the O-lattice peak.

Furthermore, the peaks at 578.8 and 588.0 eV for Cr 2p_{3/2} and Cr 2p_{1/2} were observed on 110-BiOBr adsorbed with Cr(VI) (Fig. 4c). After introducing As(V), the intensity of the Cr 2p peaks decreased remarkably owing to the competitive adsorption between CrO_4^{2-} and HAsO_4^{2-} in the interlayer. Notably, in the presence of As(III) on 110-BiOBr, the Cr 2p peaks were shifted from 578.8 and 588.0 eV to 576.6 and 586.3 eV, respectively. Meanwhile, it was worth noting that the As 3d peak of As(III) moved to 44.7 eV, towards higher binding energy. These results indicated that the potential charge transfer process of surface As(III) to interlayered Cr(VI) caused the peaks of As 3d and Cr 3d to shift in the opposite direction. Correspondingly, the Bi peaks at 159.2 and 164.5 eV indexed to Bi 4f_{5/2} and Bi 4f_{7/2}, were separately moved to 159.4 and 164.7 eV after As(III) adsorption (Fig. 4d), yet it remained almost unchanged on 110-BiOBr with adsorbed As(V). In contrast, Cr(VI) adsorption resulted in Bi 4f peaks with a 0.2-eV shift toward lower binding energy. When both were adsorbed on 110-BiOBr, the Bi 4f peaks returned to their initial positions. According to the distinct adsorption models of Cr(VI) and As(III), two kinds of affinity binding might form on the {110} facet concurrently, including surface Bi-O-As(OH)₂ and interlayer $[\text{BiO-CrO}_4\text{-BiO}]$, connecting the $[\text{Bi}_2\text{O}_2]^{2+}$ layer together. Therefore, the interfacial coupling on the {110} facet could be constructed between external As(III) and internal Cr(VI).

3.4. Simultaneous removal of Cr(VI) and As(III) by 110-BiOBr

The performance of 110-BiOBr for photocatalytic Cr(VI) reduction and As(III) oxidation was systematically evaluated at pH 7 under visible light at $\lambda > 420$ nm. Approximately 51.1% of Cr(VI) was reduced in the 110-BiOBr suspensions after 120-minutes of illumination. However, the removal efficiency of Cr(VI) increased to 71.0% in the presence of As(III) (Fig. 5a), whereas only 35.2% of Cr(VI) was reduced after the introduction of As(V). Additionally, compared with As(III) removal as low as 39.1% in the absence of Cr(VI), As(III) was almost completely oxidized to As(V) within 30 min (93.7%) in a mixture of both (Fig. 5b). The corresponding As(V) concentration in solution have a steep rise at

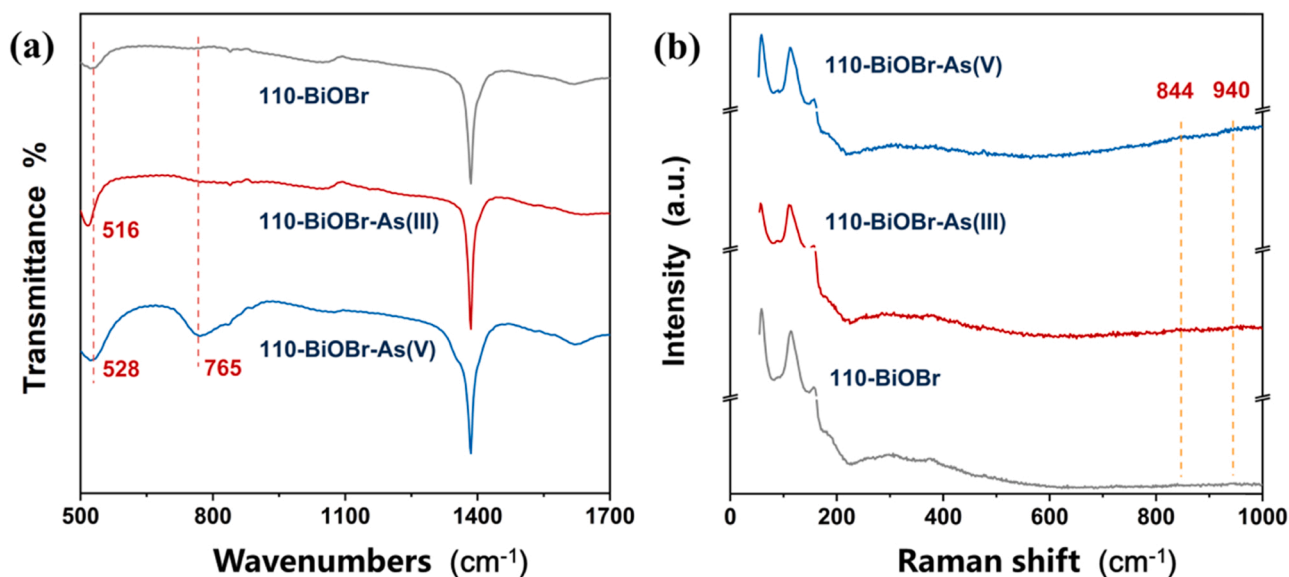


Fig. 3. FTIR (a) and Raman (b) spectrum of 110-BiOBr before and after As(III) and As(V) adsorption. All samples were obtained in solution at pH 7.0 (initial arsenic concentration was 10 mg/L; the adsorbent dose was 0.4 g/L).

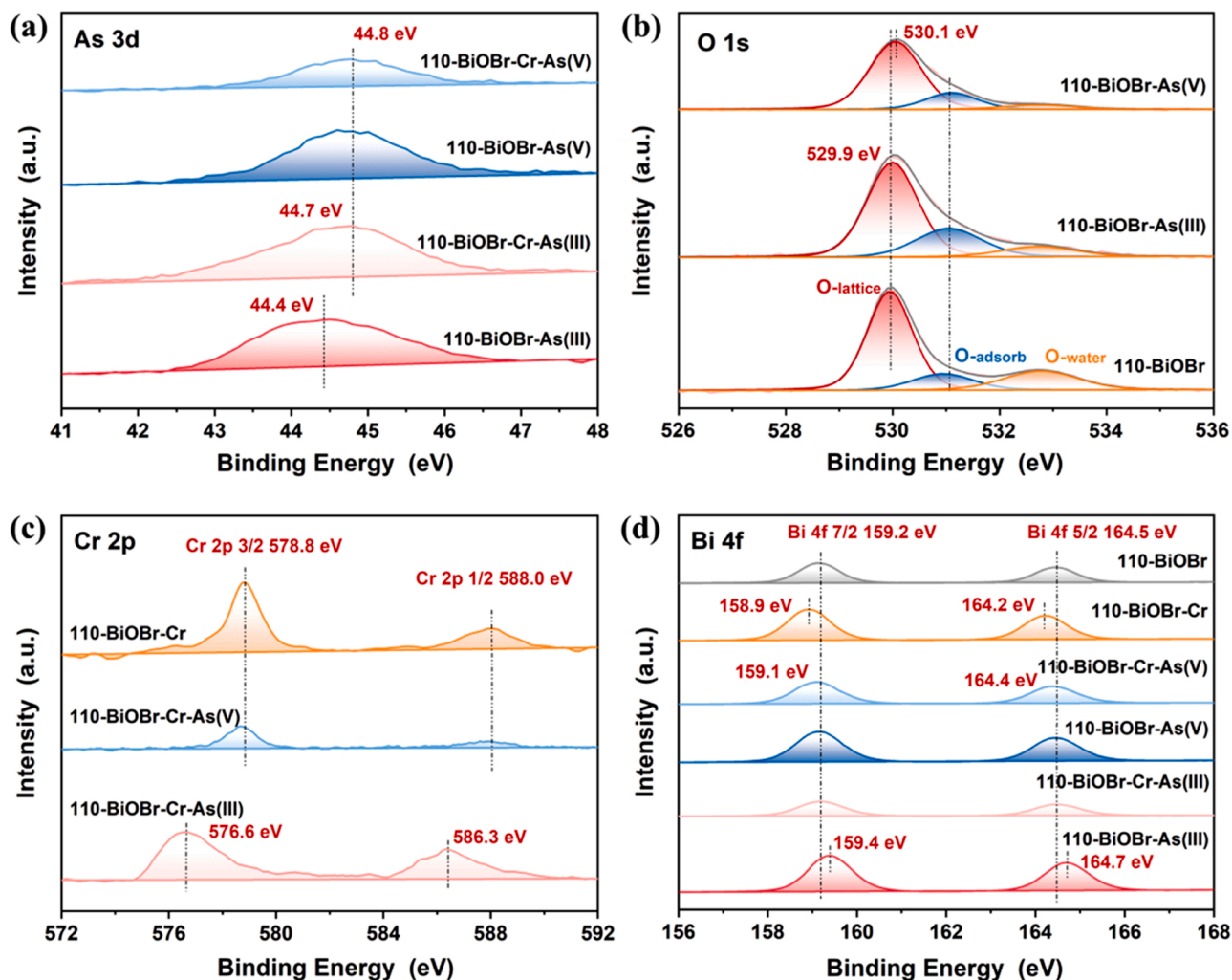


Fig. 4. As 3d (a), O 1s (b), Cr 2p (c) and Bi 4f (d) XPS spectra of 110-BiOBr with As(III), As(V) and Cr(VI) adsorption.

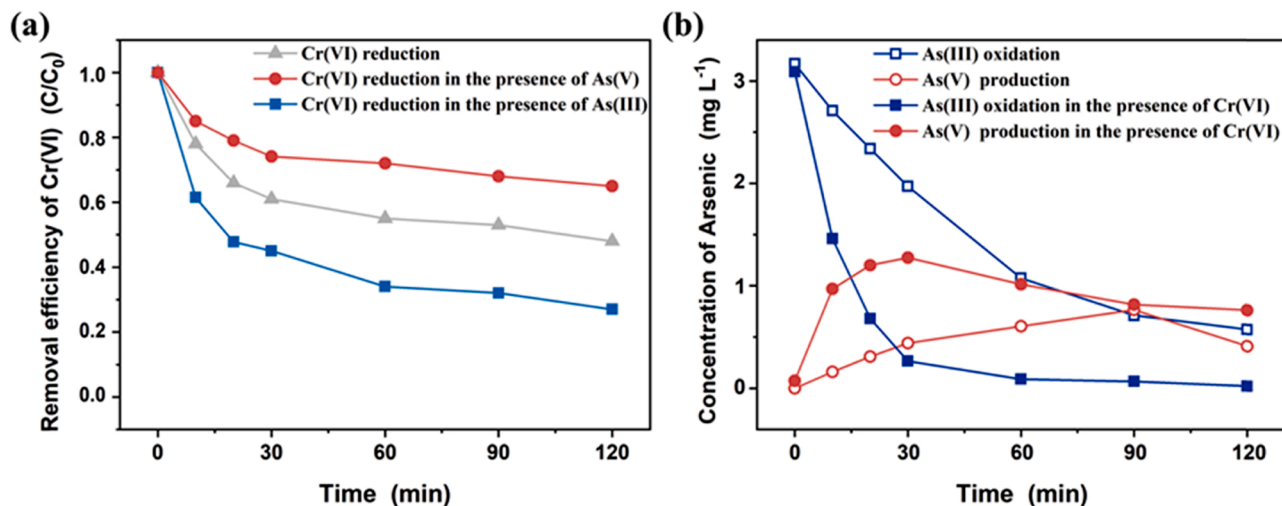


Fig. 5. Photocatalytic Cr(VI) reduction in the presence of As(III) and As(V) over 110-BiOBr at pH 7.0 under visible light irradiation ($\lambda > 420$ nm) (a) and corresponding concentration change of As(III) and As(V) during the process of Cr(VI) reduction in the coexistence system (b) (The initial Cr(VI), As(III), and As(V) concentration was 10 mg/L).

30 min at the beginning to 1.3 mg/L, and then slowly declined to 0.9 mg/L after 120 min. The higher conversion efficiency of Cr(VI) and As(III) under coexistent conditions indicated a cooperative behavior

between surface As(III) and interlayer Cr(VI), which greatly promoted the heterogeneous charge transfer. The intercalated CrO_4^{2-} between layers provided dual impurity levels of O 2p and Cr 3d states in the

energy band structure of 110-BiOBr, facilitating the direct transfer of photoexcited electrons into the Cr 3d states for Cr(VI) reduction [26]. Meanwhile, extensive uncombined photo-generated holes were produced on the oxygen sites of the $[\text{Bi}_2\text{O}_2]^{2+}$ layers, which is responsible for oxidizing As(III) adsorbed on the surface. Considering the above-mentioned interfacial coupling structure ($[\text{BiO-CrO}_4\text{-OBi}]\text{-O-As(OH)}_2$), Cr(VI) reduction occurring in the interlayer was particularly prone to induce direct electron injection derived from surface As(III), which effectively accelerated the simultaneous Cr(VI) reduction and As(III) oxidation. Moreover, owing to the interlayer anion exchange, the existence of As(V) significantly inhibited Cr(VI) reduction, suggesting intensely competitive adsorption between Cr(VI) and As(V). Upon reducing negative CrO_4^{2-} to positive Cr^{3+} , causing a change in the interlayer charge, the subsequently formed As(V) (HAsO_4^{2-}) was intercalated into the interlayer by anion exchange. As a result, the As(V) concentration in the solution first rose and then sharply dropped along with a gradual decrease in the Cr(VI) concentration. In contrast, similar phenomena, including synergistic catalysis and competitive adsorption, were not observed on BiOBr exposed with {001} facet (Fig. S7). Therefore, the simultaneous removal of Cr(VI) and As(III) depends significantly on the interlayer space related to the high exposure percentage of {110} facets for anion exchange, which constructed the coupled interface connecting the surface and interlayer. In order to investigate the stability of 110-BiOBr, the samples after reaction were characterized by XRD, and the release of Bi^{3+} and Br^- ion was measured during the simultaneous Cr(VI) reduction and As(III) oxidation processes. The Bi^{3+} ion was almost undetected as the reaction progressed, while Br^- ion slowly increased in solution. It could be ascribed to the possible exchange of the formed As(V) with Br^- between layers without affecting the primary structure of 110-BiOBr (Fig. S8a). The XRD results showed that the 110-BiOBr samples before and after reaction were entirely unchanged, indicating a stable crystal structure (Fig. S8b).

To further explore the formation of photogenerated holes (h^+) on 110-BiOBr with Cr(VI) adsorption, which is responsible for reactive oxygen species (ROS), EPR trapping experiments were carried out in pure water and 20% of methanol solution with DMPO, respectively. A typical 1:2:2:1 signal for DMPO- $\bullet\text{OH}$ adducts ($A_N=A_H=14.9$ G) was observed in the pristine 110-BiOBr suspensions (Fig. 6a). However, a stronger signal of DMPO- $\bullet\text{OH}$ was obtained on 110-BiOBr with Cr(VI), demonstrating that the reduction of intercalated Cr(VI) between layers induced more h^+ to promote the generation of $\bullet\text{OH}$ radicals. Methanol is a well-known scavenger of photogenerated holes. In the present study, in 20% of methanol solution, a tiny sextet signal of the spin adduct derived from DMPO- $\bullet\text{CH}_2\text{OH}$ ($A_N=16$ G, $A_H=22$ G) confirmed the direct oxidation of methanol by h^+ (Fig. 6b). Moreover, an

approximately multifold increase in the DMPO- $\bullet\text{CH}_2\text{OH}$ signal was detected on 110-BiOBr with Cr(VI), suggesting that more h^+ was produced on the 110-BiOBr surface for methanol oxidation. Furthermore, both the DMPO- $\bullet\text{OH}$ and DMPO- $\bullet\text{CH}_2\text{OH}$ adducts disappeared separately in pure water and 20% of methanol solution in the presence of As(III). As a result, we concluded that more h^+ originated from Cr(VI) reduction due to photo-excited electrons transfer from O^{II} to Cr^{VI} , producing Cr^{V} and O^{I} . The O^{I} atomic site plays a vital role in exporting h^+ , which contributed to the ROS formation. However, when As(III) and Cr(VI) were both adsorbed on 110-BiOBr in the form of $[\text{BiO-CrO}_4\text{-OBi}]\text{-O-As(OH)}_2$ structure, h^+ originating from O^{I} would be transported directly to As(III) adsorbed on the surface rather than generating ROS. Therefore, the rapid charge transfer between As^{III} and Cr^{VI} could simultaneously facilitate As(III) oxidation and Cr(VI) reduction.

3.5. Desorption and separation of Cr(III) and As(V)

After the oxidation of As(III) to As(V) and reduction of Cr(VI) to Cr(III), the desorption-separation processes of Cr(III) and As(V) on 110-BiOBr by acid-base treatment were investigated. Obviously, approximately 69.3% of Cr(III) was dissolved into Cr^{3+} when the pH was as low as 2.0, whereas Cr(III) in the form of Cr(OH)_3 precipitates was deposited on the 110-BiOBr surface at $\text{pH} > 4.0$ (Fig. 7a). Accordingly, As(V) was almost undetectable in solution over a broad pH range (2.0–7.0) owing to the strong electrostatic interaction between H_2AsO_4^- and the $[\text{Bi}_2\text{O}_2]^{2+}$ layer. As a result, acid treatment is a feasible approach for Cr(III) desorption from 110-BiOBr. On the other hand, excessive Br^- ions were applied to exchange As(V) within the interlayer space for desorption and regeneration. When the Br^- ion concentration increased from 0.005 to 0.5 mol/L under neutral conditions ($\text{pH} = 7.0$), the release of As(V) gradually increased to 98.6% (Fig. 7b), indicating that Br^- ions with high concentrations could fully occupy the interlayer space to substitute As(V). Meanwhile, Cr(III) was rarely found regardless of Br^- ions concentration, demonstrating highly selective separation to some extent. Therefore, according to the constant $K_{\text{sp}}(\text{Cr(OH)}_3)$ and interlayer anion exchange properties, 110-BiOBr exhibited excellent desorption and separation capacities for Cr(III) and As(V), which is indispensable for further recycling.

4. Conclusion

This study applied 110-BiOBr possessing powerful ion-exchange properties on simultaneous removal and selective separation of chromium and arsenic. The distinct adsorption behavior of Cr(VI) intercalated between layers and As(III) adsorbed on the surface results in

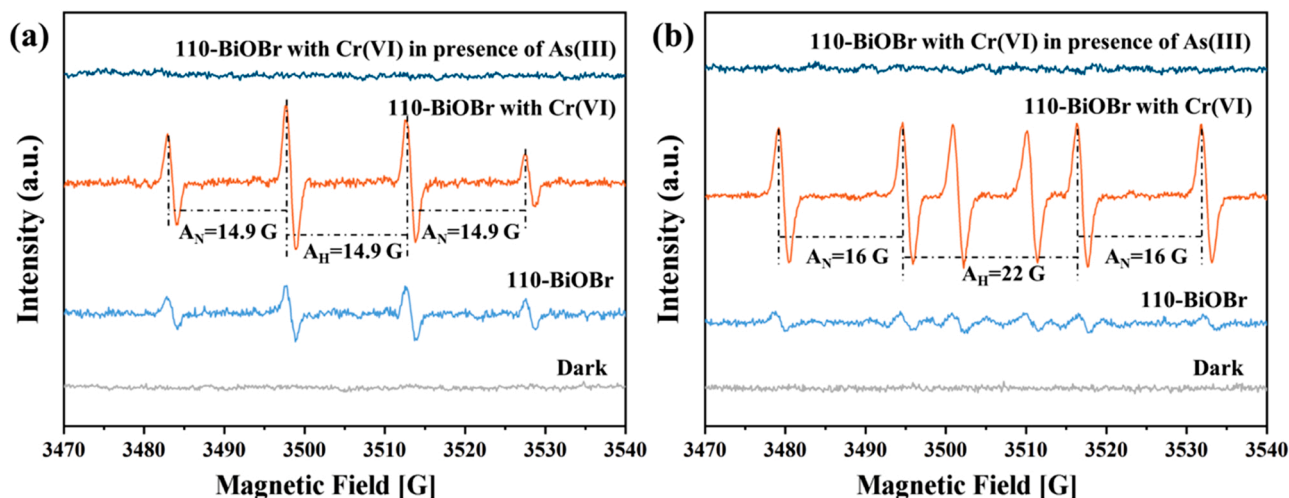


Fig. 6. In-situ irradiated EPR spectra of 110-BiOBr with Cr(VI) in the presence or absence of As(III) in pure water (a) and 20% of methanol solution (b).

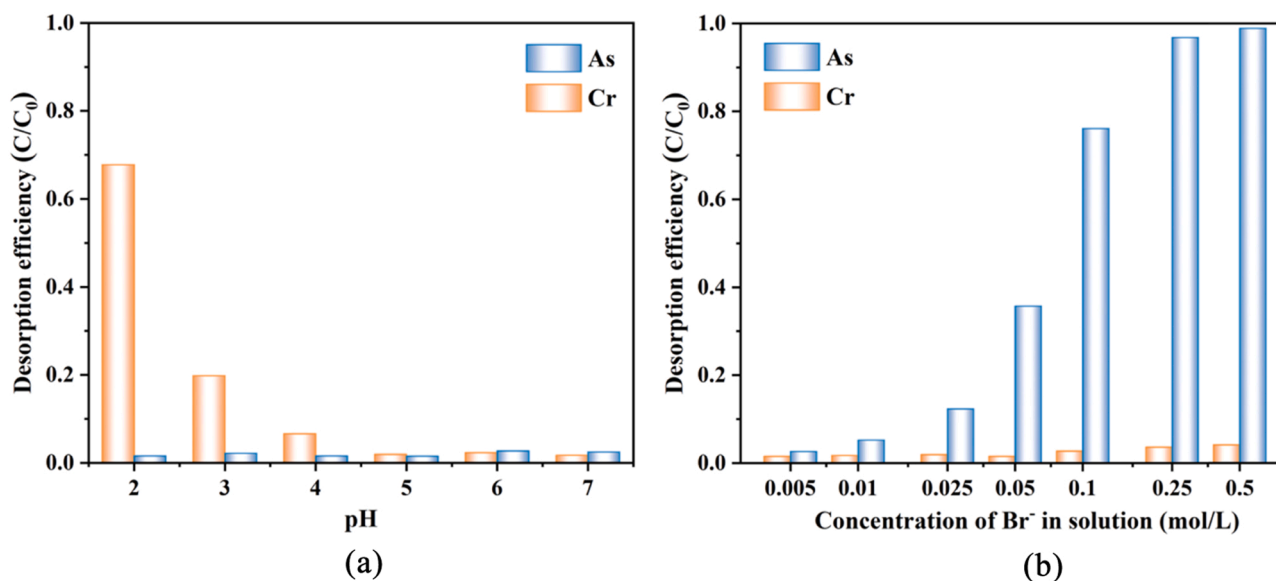


Fig. 7. Desorption of Cr(III) and As(V) on 110-BiOBr as a function of pH (a) and Br^- concentration (b) in solution after reaction.

synergic effected of As(III) oxidation and Cr(VI) reduction based on interfacial coupling structure ($[BiO-CrO_4-OBi]-O-As(OH)_2$) between the surface and interlayer on the {110} facet. Subsequently, the open-channel structure between layers not only allowed Br^- to exchange with As(V) but also enabled Cr(III) to de-intercalate under acidic conditions, thereby achieving highly selective separation of chromium and arsenic. Our findings provide a practical approach to the synergic removal and high-efficiency separation of various heavy metal ions for the application in wastewater treatment.

CRediT authorship contribution statement

Tong Li: Conceptualization, Methodology, Investigation, Data curation, Visualization, Writing – original draft, Funding acquisition, Writing – review & editing. **Lili Zhang:** Data curation, Resources. **Yaowen Gao:** Investigation, Resources. **Xueci Xing:** Software, Formal analysis. **Xiaohan Zhang:** Formal analysis. **Fan Li:** Conceptualization, Supervision, Writing – review & editing, Funding acquisition. **Chun Hu:** Conceptualization, Supervision, Funding acquisition.

Declaration of Competing Interest

The authors declare that they have no known competing financial interests or personal relationships that could have appeared to influence the work reported in this paper.

Acknowledgments

This work was supported by the National Key R&D Program of China (No. 2019YFC0408400), the National Natural Science Foundation of China (Grant Nos. 21906034, 51838005, 52100032), the China Post-doctoral Science Foundation (Grant No. 2021M700919), and the introduced innovative R&D team project under the “The Pearl River Talent Recruitment Program” of Guangdong Province (2019ZT08L387).

Appendix A. Supporting information

Supplementary data associated with this article can be found in the online version at [doi:10.1016/j.apcatb.2022.121192](https://doi.org/10.1016/j.apcatb.2022.121192).

References

- [1] D. Vilela, J. Parmar, Y. Zeng, Y. Zhao, S. Sanchez, Graphene-based microbots for toxic heavy metal removal and recovery from water, *Nano Lett.* 16 (2016) 2860–2866.
- [2] J.R. Jambeck, T. Townsend, H. Solo-Gabriele, Leaching of chromated copper arsenate (CCA)-treated wood in a simulated monofill and its potential impacts to landfill leachate, *J. Hazard. Mater.* 135 (2006) 21–31.
- [3] Y. Fu, L. Wang, W. Peng, Q. Fan, Q. Li, Y. Dong, Y. Liu, G. Boczkaj, Z. Wang, Enabling simultaneous redox transformation of toxic chromium(VI) and arsenic (III) in aqueous media—a review, *J. Hazard. Mater.* 417 (2021), 126041.
- [4] J. Luo, K. Fu, D. Yu, K.D. Hristovski, P. Westerhoff, J.C. Crittenden, Review of advances in engineering nanomaterial adsorbents for metal removal and recovery from water: synthesis and microstructure impacts, *ACS ES&T Eng.* 1 (2021) 623–661.
- [5] J. Luo, D. Yu, K.D. Hristovski, K. Fu, Y. Shen, P. Westerhoff, J.C. Crittenden, Critical review of advances in engineering nanomaterial adsorbents for metal removal and recovery from water: mechanism identification and engineering design, *Environ. Sci. Technol.* 55 (2021) 4287–4304.
- [6] M. Jian, H. Wang, R. Liu, J. Qu, H. Wang, X. Zhang, Self-assembled one-dimensional $MnO_2@zeolitic\ imidazolate\ framework-8$ nanostructures for highly efficient arsenite removal, *Environ. Sci. Nano* 3 (2016) 1186–1194.
- [7] K. Kim, W. Choi, Enhanced redox conversion of chromate and arsenite in ice, *Environ. Sci. Technol.* 45 (2011) 2202–2208.
- [8] M. Sun, G. Zhang, Y. Qin, M. Cao, Y. Liu, J. Li, J. Qu, H. Liu, Redox conversion of chromium(VI) and arsenic(III) with the intermediates of chromium(V) and arsenic (IV) via AuPd/CNTs electrocatalysis in acid aqueous solution, *Environ. Sci. Technol.* 49 (2015) 9289–9297.
- [9] Q. Ji, D. Yu, G. Zhang, H. Lan, H. Liu, J. Qu, Microfluidic flow through polyaniline supported by lamellar-structured graphene for mass-transfer-enhanced electrocatalytic reduction of hexavalent chromium, *Environ. Sci. Technol.* 49 (2015) 13534–13541.
- [10] Y.-S. Han, C.-M. Lee, C.-M. Chon, J.A. Kwon, J.-H. Park, Y.-J. Shin, D.-H. Lim, Enhanced oxidation resistance of NaBH₄-treated mackinawite (FeS): application to Cr(VI) and As(III) removal, *Chem. Eng. J.* 353 (2018) 890–899.
- [11] E.B. Cerkez, N. Bhandari, R.J. Reeder, D.R. Strongin, Coupled redox transformation of chromate and arsenite on ferrihydrite, *Environ. Sci. Technol.* 49 (2015) 2858–2866.
- [12] B. Jiang, J. Guo, Z. Wang, X. Zheng, J. Zheng, W. Wu, M. Wu, Q. Xue, A green approach towards simultaneous remediations of chromium(VI) and arsenic(III) in aqueous solution, *Chem. Eng. J.* 262 (2015) 1144–1151.
- [13] X. Guan, J. Du, X. Meng, Y. Sun, B. Sun, Q. Hu, Application of titanium dioxide in arsenic removal from water: a review, *J. Hazard. Mater.* 215–216 (2012) 1–16.
- [14] K. Gao, J. Chen, Z. Liu, Y. Li, Y. Wu, J. Zhao, P. Na, Intensified redox co-conversion of As(III) and Cr(VI) with MIL-125(Ti)-derived COOH functionalized TiO_2 : performance and mechanism, *Chem. Eng. J.* 360 (2019) 1223–1232.
- [15] L. Yan, Y. Huang, J. Cui, C. Jing, Simultaneous As(III) and Cd removal from copper smelting wastewater using granular TiO_2 columns, *Water Res.* 68 (2015) 572–579.
- [16] Z. Xu, C. Jin, F. Li, X. Meng, Mechanisms of photocatalytic degradation of monomethylarsonic and dimethylarsinic acids using nanocrystalline titanium dioxide, *Environ. Sci. Technol.* 42 (2008) 2349–2354.
- [17] Z. Wang, M. Murugananthan, Y. Zhang, Graphitic carbon nitride based photocatalysis for redox conversion of arsenic(III) and chromium(VI) in acid aqueous solution, *Appl. Catal. B Environ.* 248 (2019) 349–356.

- [18] H. Dong, Y. Zuo, N. Song, S. Hong, M. Xiao, D. Zhu, J. Sun, G. Chen, C. Li, Bimetallic synergetic regulating effect on electronic structure in cobalt/vanadium co-doped carbon nitride for boosting photocatalytic performance, *Appl. Catal. B Environ.* 287 (2021), 119954.
- [19] C. Li, H. Wu, D. Zhu, T. Zhou, M. Yan, G. Chen, J. Sun, G. Dai, F. Ge, H. Dong, High-efficient charge separation driven directionally by pyridine rings grafted on carbon nitride edge for boosting photocatalytic hydrogen evolution, *Appl. Catal. B Environ.* 297 (2021), 120433.
- [20] W. Zhang, F. Liu, Y. Sun, J. Zhang, Z. Hao, Simultaneous redox conversion and sequestration of chromate(VI) and arsenite(III) by iron(III)-alginate based photocatalysis, *Appl. Catal. B Environ.* 259 (2019).
- [21] Z. Li, S. Deng, G. Yu, J. Huang, V.C. Lim, As(V) and As(III) removal from water by a Ce-Ti oxide adsorbent: behavior and mechanism, *Chem. Eng. J.* 161 (2010) 106–113.
- [22] N. Zhu, T. Yan, J. Qiao, H. Cao, Adsorption of arsenic, phosphorus and chromium by bismuth impregnated biochar: adsorption mechanism and depleted adsorbent utilization, *Chemosphere* 164 (2016) 32–40.
- [23] T. Li, G. Zhang, H. Lan, H. Liu, J. Qu, Enhanced photoreduction of chromium(VI) intercalated ion exchange in BiOBr_{0.75}I_{0.25} layers structure by bulk charge transfer, *ACS Sustain. Chem. Eng.* 7 (2018) 2429–2436.
- [24] L. Jia, W. Zhou, X. Huang, Y. Zhang, Q. Zhang, X. Tan, T. Yu, Enhanced adsorption of Cr(VI) on BiOBr under alkaline conditions: interlayer anion exchange, *Environ. Sci. Nano* 6 (2019) 3601–3610.
- [25] J. Jiang, K. Zhao, X. Xiao, L. Zhang, Synthesis and facet-dependent photoreactivity of BiOCl single-crystalline nanosheets, *J. Am. Chem. Soc.* 134 (2012) 4473–4476.
- [26] T. Li, Y. Gao, L. Zhang, X. Xing, X. Huang, F. Li, Y. Jin, C. Hu, Enhanced Cr(VI) reduction by direct transfer of photo-generated electrons to Cr 3d orbitals in CrO₄²⁻-intercalated BiOBr with exposed (110) facets, *Appl. Catal. B Environ.* 277 (2020).
- [27] B. Xu, H. Chakraborty, V.K. Yadav, Z. Zhang, M.L. Klein, S. Ren, Tunable two-dimensional interfacial coupling in molecular heterostructures, *Nat. Commun.* 8 (2017) 312.
- [28] M. Guan, C. Xiao, J. Zhang, S. Fan, R. An, Q. Cheng, J. Xie, M. Zhou, B. Ye, Y. Xie, Vacancy associates promoting solar-driven photocatalytic activity of ultrathin bismuth oxychloride nanosheets, *J. Am. Chem. Soc.* 135 (2013) 10411–10417.
- [29] J. Li, L. Zhang, Y. Li, Y. Yu, Synthesis and internal electric field dependent photoreactivity of Bi₂O₃Cl single-crystalline nanosheets with high {001} facet exposure percentages, *Nanoscale* 6 (2014) 167–171.
- [30] J. Li, L. Cai, J. Shang, Y. Yu, L. Zhang, Giant enhancement of internal electric field boosting bulk charge separation for photocatalysis, *Adv. Mater.* 28 (2016) 4059–4064.
- [31] G. Zhang, J. Qu, H. Liu, R. Liu, G. Li, Removal mechanism of As(III) by a novel Fe-Mn binary oxide adsorbent: oxidation and sorption, *Environ. Sci. Technol.* 41 (2007) 4613–4619.
- [32] J. Kuncewicz, P. Zabek, K. Kruczała, K. Szaciłowski, W. Macyk, Photocatalysis involving a visible light-induced hole injection in a chromate(VI)–TiO₂ system, *J. Phys. Chem. C* 116 (2012) 21762–21770.
- [33] S. Wang, H. Lan, H. Liu, J. Qu, Fabrication of FeOOH hollow microboxes for purification of heavy metal-contaminated water, *Phys. Chem. Chem. Phys.* 18 (2016) 9437–9445.
- [34] J. Li, Y. Yu, L. Zhang, Bismuth oxyhalide nanomaterials: layered structures meet photocatalysis, *Nanoscale* 6 (2014) 8473–8488.
- [35] G. Zhang, F. Liu, H. Liu, J. Qu, R. Liu, Respective role of Fe and Mn oxide contents for arsenic sorption in iron and manganese binary oxide: an X-ray absorption spectroscopy investigation, *Environ. Sci. Technol.* 48 (2014) 10316–10322.
- [36] H. Wang, S. Chen, D. Yong, X. Zhang, S. Li, W. Shao, X. Sun, B. Pan, Y. Xie, Giant electron-hole interactions in confined layered structures for molecular oxygen activation, *J. Am. Chem. Soc.* 139 (2017) 4737–4742.
- [37] H. Wang, D. Yong, S. Chen, S. Jiang, X. Zhang, W. Shao, Q. Zhang, W. Yan, B. Pan, Y. Xie, Oxygen-vacancy-mediated exciton dissociation in BiOBr for boosting charge-carrier-involved molecular oxygen activation, *J. Am. Chem. Soc.* 140 (2018) 1760–1766.